Journal of Materials Chemistry A

Accepted Manuscript

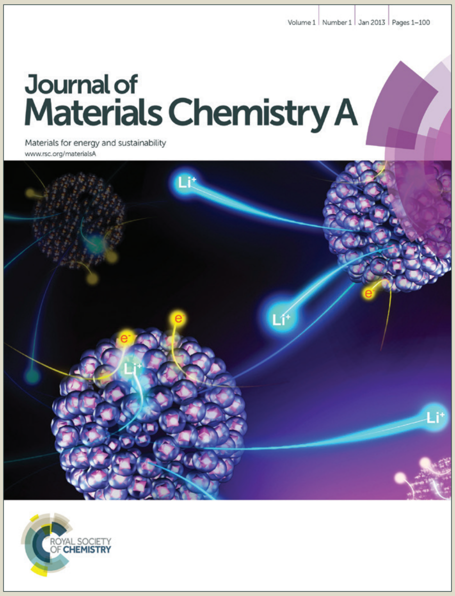

This is an *Accepted Manuscript*, which has been through the Royal Society of Chemistry peer review process and has been accepted for publication.

Accepted Manuscripts are published online shortly after acceptance, before technical editing, formatting and proof reading. Using this free service, authors can make their results available to the community, in citable form, before we publish the edited article. We will replace this *Accepted Manuscript* with the edited and formatted *Advance Article* as soon as it is available.

You can find more information about *Accepted Manuscripts* in the Information for Authors.

Please note that technical editing may introduce minor changes to the text and/or graphics, which may alter content. The journal's standard Terms & Conditions and the Ethical guidelines still apply. In no event shall the Royal Society of Chemistry be held responsible for any errors or omissions in this *Accepted Manuscript* or any consequences arising from the use of any information it contains.

ROYAL SOCIETY OF CHEMISTRY

www.rsc.org/materialsA

CREATED USING THE RSC LaTeX PCCP ARTICLE TEMPLATE – SEE www.rsc.org/electronicfiles FOR DETAILS

Prediction of high thermoelectric potential in $\mathrm{AMN_2}$ layered nitrides: electronic structure, phonons, and anharmonic effects[†]

Rabih Al Rahal Al Orabi,[*a] **Ester Orisakwe,**[b] **Daehyun Wee,**[a] **Bruno Fontaine,**[b] **Régis Gautier,**[b] **Jean-François Halet,**[b] **and Marco Fornari** [*c]

Received Xth XXXXXXXXXX 20XX, Accepted Xth XXXXXXXXX 20XX
First published on the web Xth XXXXXXXXXX 200X
DOI: 10.1039/b000000x

Band structures, electronic transport coefficients, harmonic and anharmonic vibrational properties of novel layered nitrides have been studied to evaluate the potential for thermoelectric applications. Using first principles theoretical methods we predict that $\mathrm{AMN_2}$ compounds with A=Ca, Sr, and Ba, and M=Ti, Zr, Hf may exhibit Seebeck coefficients in excess of 150 $\frac{\mu V}{K}$ and good electrical conductivities. The phonon dispersions indicate the presence of low lying optic modes that can lead to low thermal conductivity. The analysis of the mode resolved Grüneisen parameter points to large anharmonicity. In addition, we show that the A-site substitution controls the degeneracies at the top of the valence band and the anisotropy of the Seebeck tensors.

1 Introduction

Since the pioneering work of Goldsmid and Slack in the sixties,[1–3] thermoelectric (TE) energy conversion has been the chimera of power generation, energy recovering systems, and refrigeration in nano- and macro-systems alike.[4–6]

One bottleneck to achieve competitive conversion performance is the efficiency of the active materials used to engineer the devices. These materials must satisfy several contradictory requirements both in the electrical and thermal transport channels in order to maximize the TE efficiency. Material performance is determined by the figure of merit, $ZT=\frac{S^2\sigma}{k}$, which involves the Seebeck coefficient, S, the electrical conductivity, σ, and both the electronic and lattice contribution to the thermal conductivity, $k = k_e + k_L$. Optimizing simultaneously these four transport quantities at the desired operating temperature, T, is very difficult. The free electron model helps to rationalize the difficulty of increasing the power factor (the numerator in the figure of merit, $S^2\sigma$). In fact, within the constant relaxation time approximation and in a simple isotropic model (see Ref. 7 and reference therein for a more general tensorial theory), the dependence of the conductivity and the Seebeck coefficients on the carrier density, n, and the effective mass, m^* is given by $\sigma \sim \frac{n}{m^*}$ and $S \sim \frac{m^*}{n^{2/3}}$ (in the metallic limit) indicating that viable materials must be heavily doped semiconductors with large effective masses and reasonable number of charge carriers. Good power factors are reached when $\sigma \sim \frac{10^3}{\Omega cm}$ and $S \sim 200\frac{\mu V}{K}$ (Ref. 8) and typical optimization approaches involve tuning the band structure,[9,10] the doping level,[11,12] and/or the scattering mechanisms that determine the relaxation time for the electrons, τ_e. The electronic structure also determines the electronic component of the thermal conductivity but, in normal bulk cases, the Wiedmann-Franz law sets k_e. The vibrational properties should also be concurrently optimized, with the specific goal to reduce the lattice thermal conductivity in the denominator of the figure of merit. Values near $k_L \sim 1\frac{W}{mK}$ (Ref. 8,13) are usually expected for good thermoelectric materials. In order to pinpoint the basic conundrum to optimize the vibrational properties, we can consider an anharmonic phonon gas model that gives $k_L \sim v_s \tau_p c_V$, where v_s is the speed of sound in the material, c_V the specific heat, and τ_p the scattering relaxation time for the phonons; a large v_s leads to a large Debye temperature that in turn decreases c_V. A balance must be struck also in the heat transport channel. In order to optimize k_L for thermoelectric applications, the scattering time should also be controlled by tuning the anharmonicity of the lattice and/or disrupting the crystalline order by alloying or cage-filling. The Phonon Glass-Electron Crystal (PGEC) paradigm[1] conceptualizes this last approach of reducing k_L in structures such as filled skutterudites,[14–16] chalcogenide of molybdenum clusters,[17,18] and clathrates.[19,20] Filling the cages may also im-

---

[†] Electronic Supplementary Information (ESI) available: Band structures for $\mathrm{CaHfN_2}$, $\mathrm{SrHfN_2}$ and $\mathrm{BaHfN_2}$; Densities of states for $\mathrm{CaZrN_2}$, $\mathrm{SrZrN_2}$, $\mathrm{BaZrN_2}$, $\mathrm{CaHfN_2}$, $\mathrm{SrHfN_2}$ and $\mathrm{BaHfN_2}$; Thermoelectric transport coefficients of $\mathrm{CaTiN_2}$, $\mathrm{BaTiN_2}$, $\mathrm{SrZrN_2}$, $\mathrm{CaHfN_2}$, $\mathrm{SrHfN_2}$, and $\mathrm{BaHfN_2}$; Vibration density of states of $\mathrm{CaTiN_2}$; Mode-resolved Grüneisen parameters versus mode frequency for $\mathrm{SrTiN_2}$. See DOI: 10.1039/b000000x/

[a] *Department of Environmental Science and Engineering, Ewha Womans University, Seoul, 120-750, Korea. E-mail: alrah1r@cmich.edu*
[b] *Institut des Sciences Chimiques de Rennes, UMR 6226 CNRS-Université de Rennes 1-Ecole Nationale Supérieure de Chimie de Rennes, 11 allé de Beaulieu, CS 50837, F-35708 Rennes, France.*
[c] *Department of Physics and Science of Advanced Materials Program, Central Michigan University, Mount Pleasant, Michigan 48858, USA. Fax: +1 989 774 2697; Tel:+1 989 7742564; E-mail: marco.fornari@cmich.edu*

prove the electronic properties.[16,21,22] Other materials exhibit very low bulk thermal conductivity because of intrinsic anharmonicity in the bonding.[23] It was also demonstrated that nano structuring may improve the thermoelectric energy conversion but we focus here exclusively on bulk materials.[24–30]

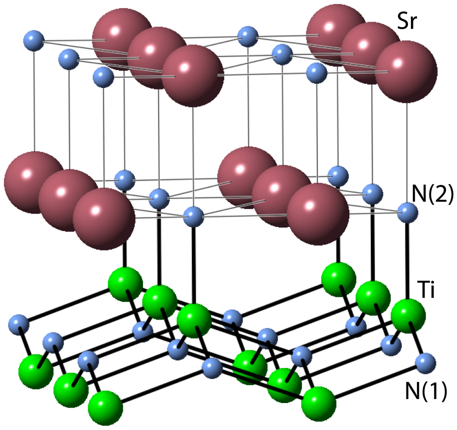

Fig. 1 Crystal structure of $SrTiN_2$ ($KCoO_2$ structure type). The unit cell contains two independent nitrogen atoms on Wyckoff positions N(1)= $(\frac{1}{4},\frac{1}{4},\frac{1}{2})$ and N(2)= $(\frac{1}{4},\frac{1}{4},z)$. Ti-N(1) layers (Ti in green and N in blue) alternate with Sr-N(2) layers (Sr in brown).

Another interesting approach to improving the overall thermoelectric performances relies on combining, in bulk materials, structural units that contribute to the macroscopic properties of the full crystal but can be optimized separately. It was argued, at least for composites, that the thermoelectric efficiency of the whole may exceed the properties of the constituents.[24] The key aspect of this approach is to optimize the properties of one constituent without compromising the contribution of the others. Layered materials provides a natural playground to explore the contribution of different units and their tuning. From the point of view of the band structure the layered structure favors anisotropic effective mass tensors with large masses associated with reduced intra-layer hopping and smaller in-plane masses that can be used to optimize the power factor. It was also shown that layered materials such as cobalites oxides,[31–33] and oxychalcogenides[34,35] exhibit low lattice thermal conductivity. The mechanism that causes the reduction of the thermal conductivity in cobaltites and rhodates[36] is vacancy scattering whereas, in oxychalcogenides, the reduction is associated the large anharmonicity in one layer.[37]

Recent research has pointed to nitrides and nitridometalates as interesting functional materials for a variety of applications ranging from high T_C superconductivity such as in Li_xMNCl (M= Zr, Hf)[38,39] to mechanical properties of ultrahard and thermally stable spinels such as A_3N_4 with A=Si, Ge, Sn.[40,41] Although the chemistry of N presents important difference with respect to the chemistry of O,[39] the nitridometalates exhibit the structural richness encountered in oxides.[42,43] The ternary AMN_2 compounds adopt, for instance, structures similar to those found in oxides and chalcogenides.[32,34,35] From the point of view of thermoelectricity the main advantage with respect to the oxides is the decreased electronegativity of N that may favor an enhanced electrical conductivity and, hence, improved performance.

In this manuscript we analyze the electronic structure, the electronic transport coefficients, and the vibrational properties of layered nitrides compounds with general formula AMN_2, specifically $SrTiN_2$, $BaZrN_2$, and $BaHfN_2$ that have been recently synthesized,[42,44,45] but also other compositions in the same family. Although one theoretical study has already been devoted to some of these compounds,[46] no complete study has yet been performed to rationalize the vibrational and electronic transport properties in these AMN_2 compounds.

2 Computational details

Our calculations are based on Density Functional Theory (DFT). For the electronic band structures we used the full-potential linearized augmented plane wave (FLAPW) approach, as implemented in the WIEN2K code.[47] The Perdew, Becke and Ernzerhof,[48] and the modified Becke-Johnson (mBJ)[49] functionals were used for the structural optimizations and the band structure calculations, respectively.

The muffin-tin radii (R_{MT}) were chosen small enough to avoid overlapping during the optimization process. A plane wave cutoff corresponding to $R_{MT}K_{max}$ = 7 was used in all calculations. The radial wave functions inside the non- overlapping muffin-tin spheres were expanded up to l_{max} =12. The charge density was Fourier expanded up to G_{max} =16 Å^{-1}. Total energy convergence was achieved with respect to the Brillouin zone (BZ) integration mesh with 500 k-points. Optimization was obtained by minimizing the total energies of their primitive cells as a function of volume according to Birch-Murnaghan equation of state:[50,51]

$$E(V) = E_0 + 9V_0B_0/16[(X^2-1)^3B_0' + (X^2-1)^2(6-4X^2)] \tag{1}$$

where V_0 represents the equilibrium volume, B_0 the bulk modulus, B_0' the bulk modulus pressure derivative, E_0 the equilibrium energy and $X = (V_0/V)^{1/3}$

The electronic transport coefficients are calculated within the Boltzmann Transport Equation (BTE) with constant τ_e and the rigid band structure approximation,[52,53] as implemented in the BoltzTrap code.[54] The electrical conductivity and power factor were calculated with respect to τ_e, whereas the Seebeck coefficient is independent of τ_e. We used 10000 k-points in the

BZ to compute the band derivatives and the density of states for the transport calculations.

Vibrational properties have been obtained by using the density functional perturbation theory (DFPT),[55] as implemented in the Quantum ESPRESSO (QE) package.[56] The calculation has been performed by using a set of ultrasoft pseudopotentials[57,58] with the PBEsol exchange-correlation functional.[59] The kinetic energy cutoff and the charge density cutoff are set to be 40 Ry and 480 Ry, respectively. A $8 \times 8 \times 4$ k-points mesh is used to sample the Brillouin zone. The dynamical matrix has been constructed on a $2 \times 2 \times 2$ q-point mesh and subsequently interpolated onto a finer mesh ($16 \times 16 \times 8$) to generate the vibrational density of states (VDOS). The Grüneisen parameters have been computed with a finite difference method, expanding isotropically the cell volume by +3% with respect to the DFT relaxed volume. The structural parameters obtained by the pseudopotential method and the FLAPW method agree each other within 1%, and the electronic band structures are comparable for most purposes.

3 Results and discussion

3.1 Structural features of AMN_2 materials

Nitrides with general formula AMN_2, such as $SrTiN_2$, $BaZrN_2$ and $BaHfN_2$, adopt the $KCoO_2$ tetragonal structure with space group *P4/nmm* (No. 129).[42] In this structure the layers containing the transition metal (M) alternate along the c-axis with the layers containing the alkaline earth (A). In $SrTiN_2$, for instance, the structure is composed of nitridotitanate $[TiN_2]^{2-}$ anions compensated by Sr^{2+} cations (two formula units per primitive cell) (Fig. 1). Within the $[TiN_2]^{2-}$ group, Ti^{4+} is coordinated to five nitrogen (four N in positions N(1) and one N in position N(2)) in a distorted square based pyramidal geometry with an overall C_{4v} point group symmetry. These polyhedra are linked through edges and the apexes of two adjacent pyramids are pointing in the opposite directions along the c-axis. The Ti^{4+} is located above the basal nitrogen plane, towards the interior of the pyramid forming an N(1)-Ti-N(1) angle of about 141 deg (Fig. 1). Because the square based pyramids are compressed along the c axis, the $[TiN2]^{2-}$ layers contain four long basal Ti-N(1) bonds at 2.024 $Å$ and one shorter apical Ti-N(2) bond at 1.836 $Å$. Sr and N(2) form a rocksalt-like layer with the cations in square pyramidal coordination with five N atoms. The average distance Sr-N(2) is equal to 2.66 $Å$ and is of the same order of magnitude as that found in other strontium ternary nitrides.

By changing Sr with Ca the cell's $\frac{c}{a}$ parameter slightly decreases because of the smaller cation in the rocksalt layer. The Ti-N layer remains unchanged indicating that strong covalency controls the lattice parameters. In $BaTiN_2$ the lattice parameter increases of about 5% but the $\frac{c}{a}$ does not change. Combined with the larger ionic radius of Ba the bonds in the rocksalt layer are modified. Similar trends are observed for $AZrN_2$ and $AHfN_2$.

The optimized (with Wien2K) lattice parameters, cell volumes, bulk moduli as well as interatomic distances for the nine AMN_2 compounds are in Table 1. The theoretical geometries are with in 2% of the experimental structures. As expected, lattice parameters increase in accord with the ionic radii of the chemical species.

3.2 Band structure and electronic transport

The band structures are typical of ionic systems with a charge transfer energy gap that we computed between 1.6 to 2.6 eV for all compounds (Fig. 2, 3)†. The conduction band (CB) involves, as expected, transition metal d-states and alkaline earth s-states. It is interesting to point out that the lowest CB has d-character with a dispersion of almost 1.5 eV.[61] The Γ and Z points in the Brillouin zone are degenerate due to the layered structure and the corresponding effective mass for n-type transport is very anisotropic.

The valence band (VB) manifold near the energy gap is largely dominated by p-states from N(1) (lower energy) and N(2) (higher energy) (Fig. 4)†, however, transition metal d-states have reasonably large cross gap hybridization in the valence manifold. The top of the VB is N(2) in character and, in all compounds, the reduced dispersion allows to activate simultaneously several valleys for the electronic transport. The anisotropy of the effective masses and the degeneracies are controlled by the alkaline earth substitution.

Let us focus first on $ATiN_2$ (Fig. 5). The n-type thermopower, using the optimal carrier concentration, reaches values up to 400 $\frac{\mu V}{K}$ in the zz diagonal component for temperatures just above 300 K (Fig. 5c). The optimized carrier concentration correspond to a chemical potential of 2.7 eV (with respect to the top of the valence band) activating the dispersive bottom band but also higher bands that are quasi degenerate at the M-point. The multi-valley band structure should favor large S.[62] The conductivity is highly anisotropic: very small and large in the zz and xx components, respectively. This is simply a consequence of large dispersive character of the bottom of the conduction band in the transverse directions. Within our approximations only the conductivity divided by the constant scattering time can be computed. The conductivity may be strongly affected by the specific value of τ_e. The lowest energy conduction band remains substantially unchanged when replacing Ca with Sr and Sr with Ba; the Ti d-character of the lowest lying CB justifies this behavior. In turn, the n-type transport coefficient do not dramatically change although the Ba containing compounds seem less attractive.

The top of the VB in $ATiN_2$ is quite sensitive to the Ca-Sr-Ba replacement, especially at the A point which becomes,

Table 1 Optimized cell parameters (a and c), *A*-N and *M*-N bond distances, number of equivalent bonds (n), unit cell volume (V), Bulk modulus B_0 and energy band gap (E_G) of the AMN_2 compounds discussed in the text. Experimental values are also reported when available.

Compounds	a (Å)	c (Å)	*A*-N (Å)	*M*-N (Å)	n	V (Å^3)	B_0 (GPa)	E_G (eV)
$CaTiN_2$	3.807	7.517	2.355	1.836	1	108.9	127	1.70
			2.694	2.025	4			
$SrTiN_2$	3.802	7.776	2.597	1.836	1	112.4	123	1.60
			2.691	2.024	4			
$SrTiN_2$ (exp)[42]	3.880	7.776	2.581	1.839	1	116	-	
			2.745	2.056	4			
$BaTiN_2$	4.014	8.068	2.845	1.826	1	130.0	101	1.40
			2.939	2.106	4			
$CaZrN_2$	3.996	8.131	2.275	2.011	1	129.8	129.8	2.20
			2.832	2.159	4			
$SrZrN_2$	4.069	8.296	2.523	2.017	1	137.3	122	2.00
			2.882	2.180	4			
$BaZrN_2$	4.188	8.502	2.727	2.001	1	149.1	124	1.80
			2.948	2.207	4			
$BaZrN_2$ (exp)[60]	4.161	8.392	2.771	2.011	1	145.3	-	
			2.948	2.202	4			
$CaHfN_2$	3.960	8.150	2.302	2.017	1	127.8	128	2.60
			2.808	2.137	4			
$SrHfN_2$	4.043	8.278	2.540	2.008	1	135.3	123	2.40
			2.865	2.161	4			
$BaHfN_2$	4.152	8.491	2.819	1.993	1	146.4	106	2.10
			2.946	2.199	4			
$BaHfN_2$ (exp)[44]	4.128	8.382	2.680	2.050	1	142.8	-	
			2.922	2.186	4			

in $BaTiN_2$, degenerate with the Γ, M, and Z points. This behavior can be rationalized in term of changes in the A-N(2) hybridization with the increase of the ionic size of the A-ions. The p-type Seebeck coefficient is very promising for $SrTiN_2$ with values in excess of 200 $\frac{\mu V}{K}$ above 500 K. (Fig. 5a) Also, the average values of the electrical conductivity for p-type doping may indicate thermoelectric promise if τ_e attains reasonable values (Fig. 5b). A very interesting point discussed by Ref. 63 is related to the link between anisotropy of the Seebeck tensors and the band structure. When the band extrema contributing to the transport coefficients have the same energy, the Seebeck tensor is proportional to the identity. However, when such a degeneracy is removed and the band extrema are shifted in energy with respect to each other, the diagonal terms of the Seebeck tensor may differ favoring anisotropy. Indeed, at the top of the VB the Γ, M, Z, and A points undergo small energy shifts that affect the band degeneracies. This change in the degeneracies determines the spread of the diagonal terms of the Seebeck coefficient that must be zero in the case of perfect degeneracy. The effect is observed in Fig. 5 which show that S is, to a greater extent, a multiple of the identity matrix in the case of a multi valley band structures with degenerate extremes. Due to the presence of several non-degenerate extreme contributing to the transport the effect is not observed for $CaZrN_2$.

Similar considerations on the transport coefficients apply to $AZrN_2$-compounds and $AHfN_2$-compounds (Fig. 6, 7,)†. However, with Zr, and Hf the CB manifold is less disperse and the forbidden energy gap decreases slightly, see Table 1. It worthwhile to notice that the mBJ functional used for the electronic structure calculations usually leads to excellent agreement with the experimental values for the HOMO-LUMO energy gap. The top of the VB exhibits features similar to $ATiN_2$ with similar interplay between the diagonal terms of the Seebeck coefficient and band degeneracies and the results are consistent with the prediction of the models.[7]

3.3 Vibrational properties

The phonon dispersions for the $ATiN_2$ series are in Fig. 8. The phonon spectrum does not provide direct information on the heat transport but is a starting point to discuss, at least phenomenologically, the possible scattering channels and the tuning strategies related to the thermal conductivity. Phonon frequencies at the Brillouin zone center can be used to interpret IR and Raman experiments. The acoustic phonons are the most important for thermal transport because of the larger sound velocity. Low-energy optic modes, however, are a pos-

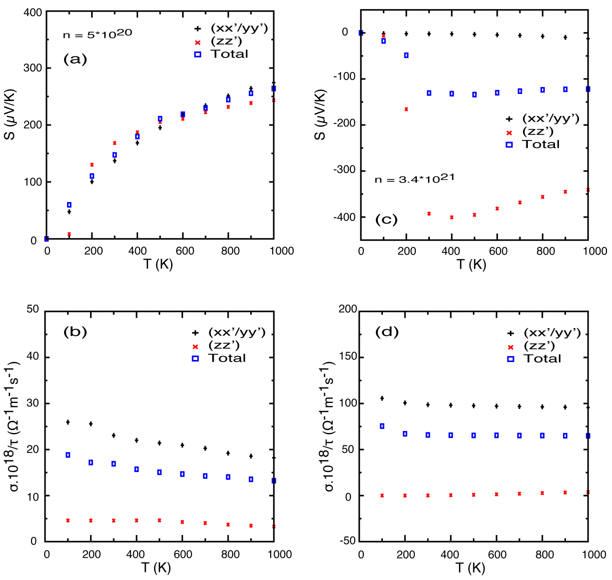

Fig. 5 Thermoelectric transport coefficients of $SrTiN_2$ as a function of temperature at the optimal carrier concentration (n): (a) p-type Seebeck coefficient; (b) p-type electrical conductivity divided by the constant relaxation time; (c) n-type Seebeck coefficient; (d) n-type electrical conductivity divided by the constant relaxation time.

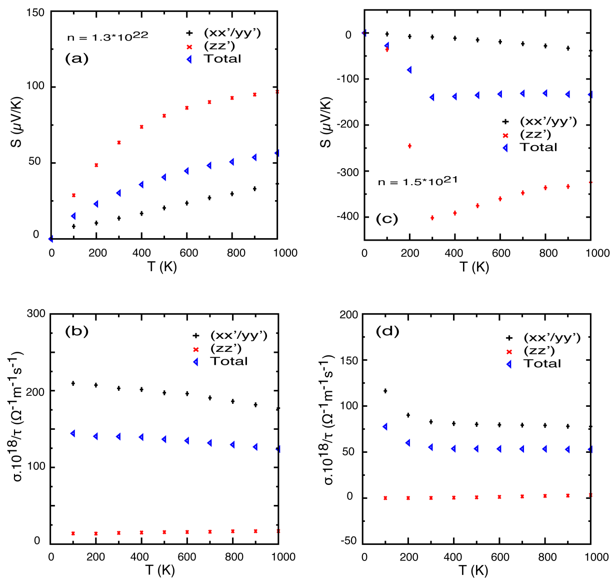

Fig. 6 Thermoelectric transport coefficients of $CaZrN_2$ as a function of temperature at the optimal carrier concentration (n): (a) p-type Seebeck coefficient; (b) p-type electrical conductivity divided by the constant relaxation time; (c) n-type Seebeck coefficient; (d) n-type electrical conductivity divided by the constant relaxation time.

sible source of scattering and should also be considered carefully when aiming to lower the thermal conductivity.[3]

For all the $ATiN_2$ compounds, modes with frequency below 100 cm^{-1} mostly involves A-ions vibrations. With the lightest alkaline earth (Ca), the vibrations in this frequency region are mostly in-plane with out-of-plane contribution starting at higher frequency. The Sr and the Ba substitution obviously lowers the frequency but also add a substantial out-of-plane contribution in this spectral region (Fig. 9, 10)†. The presence of optic vibrations near 80 cm^{-1} in $BaTiN_2$ may lead to low lattice thermal conductivity. By analyzing the vibrations of N(1) and N(2) anions, two important frequency regions can be recognized: (1) at lower frequency (roughly below 400-500 cm^{-1} the N(1) vibrations are largely out-of-plane motion whereas the N(2) vibrations are in-plane; (2) at higher frequency the character of the N(1) and N(2) vibrations is reversed. In region (1) the peak associated with the bond bridging the layers and involving Ti and N(2) is clearly recognizable at 350 cm^{-1} in $CaTiN_2$, at 300 cm^{-1} in $SrTiN_2$, and 250 cm^{-1} in $BaTiN_2$. The Ti is involved mostly in vibrations in region (1).

The layer-by-layer decomposition of the modes indicates a larger intra-layer contribution (perpendicular to the c-axis) to the the vibrations that is consistent with the layered structure. The vibrations along the c-axis gain more weight for the heavier alkaline earths. The Ti-layer has minor contribution on the modes below 100 cm^{-1} and does not contribute greatly to the heat-carrier vibrations. The A-layers, on the other hand, involves low frequency modes, both acoustic and optic that can contribute to phonon-phonon scattering mechanisms.

The Born Effective Charges (BEC)[55] provide an insight on the electronic response to atomic vibrations and may shed light on covalency of bonds. In Table 2 we report the diagonal components of the BEC tensors for all the elements in $CaTiN_2$, $SrTiN_2$, and $BaTiN_2$. The alkaline earths BECs decrease in anisotropy when increasing the ionic size of the alkaline earth ion, the Ti BECs also follows similar trends and are quite large because of the substantial *d* cross-gap hybridization in the valence band. As noted by Pickett[61] the BECs of N(1) and N(2) ions substantially deviates from the formal charge. N(1)'s BEC tensors provide additional evidence of the Ti-N covalence whereas N(2)'s BEC tensors have much larger values in the *z* component, however, such an anisotropy decreases for the Ba compound.

In order to estimate the anharmonicity of the vibrations and the possible effect of lowering the thermal conductivity we have computed the Grüneisen parameters $\gamma_{\mathbf{q}s}= -\frac{d\ln\omega_{\mathbf{q}s}}{d\ln V}$ for each atom in the unit cell (Table 3). The small values associated with Ti point, again, to the rigid bonds in Ti environment. The smaller alkaline earths are more sensitive to volume changes than the larger Ba. For comparison, values computed in BiCuOS are 0.19, 0.22, 0.43, 0.48 for Bi, O, Cu, and S respectively. Overall the thermal conductivity is not expected to be as low as the layered oxychalcogenides.

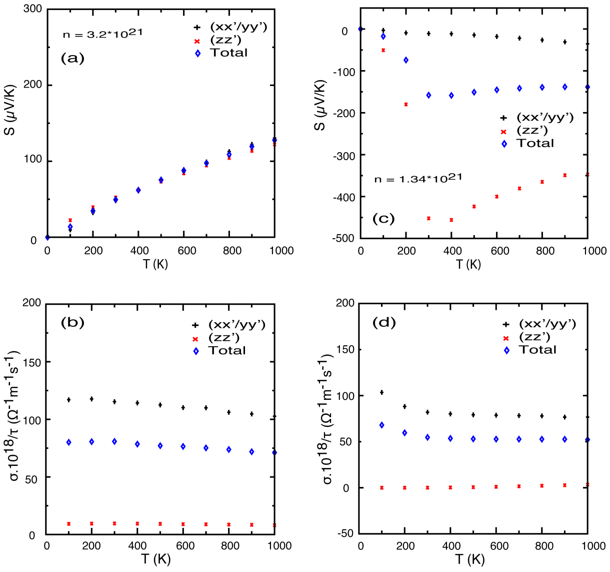

Fig. 7 Thermoelectric transport coefficients of $BaZrN_2$ as a function of temperature at the optimal carrier concentration (n): (a) p-type Seebeck coefficient; (b) p-type electrical conductivity divided by the constant relaxation time; (c) n-type Seebeck coefficient; (d) n-type electrical conductivity divided by the constant relaxation time.

The Grüneisen parameter, γ, was calculated to be equal to 1.58, 1.30 and 1.40 for $CaTiN_2$, $SrTiN_2$ and $BaTiN_2$, respectively. These parameters represent a measure of the bonding anharmonicity and govern the phonon-phonon scattering rate, which is proportional to γ^2.[64] Large γ values are indicative of high anharmonicity and reflect stronger phonon scattering, that is, lower thermal conductivity. These values are close than those found in PbTe ($\gamma = 1.45$), $AgSbTe_2$ ($\gamma = 2.05$) and $Ag_2Tl_2Mo_9Se_{11}$ ($\gamma = 0.9$) whose measured thermal conductivities at room temperature are 2.4, 0.68 and 0.6 in unit of $\frac{W}{mK}$, respectively.[22,65,66] In $CaTiN_2$, $SrTiN_2$ and $BaTiN_2$ the larger contribution to the Grüneisen parameter is attributed to low frequency modes, Fig. 11[†]. Larger values are computed for $CaTiN_2$ near 100 cm^{-1} and corresponding mostly to in-plane vibrations. In $SrTiN_2$ the Grüneisen parameters distribution flattens whereas in $BaTiN_2$ the largest "anharmonicity" is associated to in all directions Ba-vibrations. This trends can be rationalized in terms of volume available to the vibrations that changes with the A-site substitution. It is interesting to notice the peak at at 250 cm^{-1} that we associated with the horizontal distortion of the Ti-N(2) bond.

4 Conclusions

We have compared the electronic structure, charge transport properties, and the vibrational spectra of layered nitrides, AMN_2, to consider their potential for thermoelectric applications. These materials are formed by M-N layers and A-N layers alternating along the c-axis. The M-N bonds have large degree of covalence that may favor the electronic transport. The A-N has rock-salt structure and is largely ionic especially with Ca and Sr. The band structure exhibit strongly anisotropy and large effective masses that are known to favor large Seebeck coefficients. The degeneracies between the valence band maxima are controlled by the alkaline earth: when the maxima are degenerate the Seebeck tensors is proportional to the identity matrix. The Born effective charges are unusually large and anisotropic for N. An analysis of the vibrational properties further underline the large contribution of in-plane vibrations. Low sound velocity and optic mode below 100 cm^{-1} justify the expectation for low thermal conductivity. The properties may be further tuned by mixing Ba and Sr in the rock-salt layer.[‡]

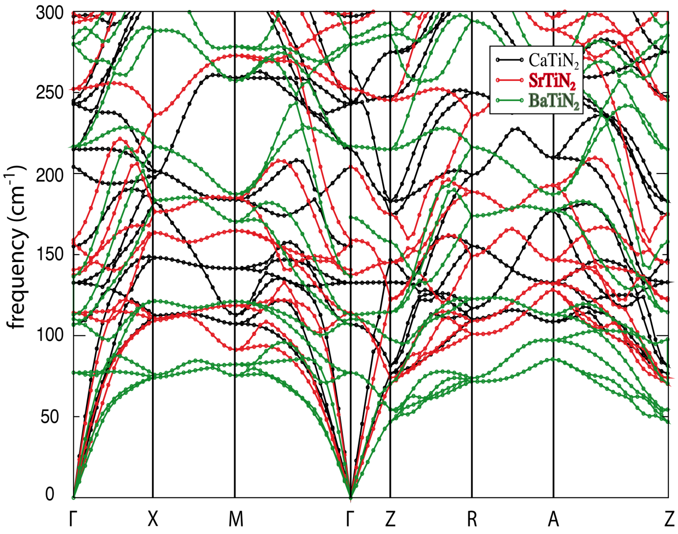

Fig. 8 Phonon dispersions for $CaTiN_2$ (black), $SrTiN_2$ (red) and $BaTiN_2$ (green).

References

1 *in Thermoelectrics Handbook : Macro to Nano, Eds., D. M. Rowe, CRC Press*, ed. G. A. Slack, 1995.
2 *In Thermoelectric Nanomaterials*, ed. T. Koumoto, K.and Mori, 2013.
3 G. S. Nolas, J. Sharp and J. Goldsmid, *Thermoelectrics: Basic Principles and New Materials Developments*, Springer Series in Materials Science, Berlin, 2001, vol. 45.
4 L. E. Bell, *Science*, 2008, **321**, 1457–1461.

[‡] We are grateful to Dr. Nicholas Mecholsky for a careful reading of the manuscript and useful discussions. The authors thank Solvay Special Chemicals for financial support. Computations were partially performed at the High Performance Computing Center at Michigan State University. MF acknowledges collaboration with the AFLOW Consortium (`http://www.aflowlib.org`) under the sponsorship of DOD-ONR (N000141310635).

Table 2 Effective charges computed with density functional perturbation theory.

Compounds	Atoms	E_x=E_y	E_z
$CaTiN_2$	Ca	2.32357	3.05531
	Ti	4.99157	3.41473
	N1	-5.27722	-1.64637
	N2	-2.03066	-4.82882
$SrTiN_2$	Sr	2.43354	2.96640
	Ti	5.04181	3.14575
	N1	-5.24901	-1.57900
	N2	-2.21996	-4.58575
$BaTiN_2$	Ba	2.85986	2.96484
	Ti	5.00298	2.66289
	N1	-5.29989	-1.39959
	N2	-2.55192	-4.32231

Table 3 Grüneisen parameters of AMN_2, n is the number of atoms in the cell.

Compounds	Atoms	n	Grüneisen parameters
$CaTiN_2$	Ca	2	0.241
	Ti	2	0.08
	N1	2	0.225
	N2	2	0.242
Total		8	1.576
$SrTiN_2$	Sr	2	0.16
	Ti	2	0.08
	N1	2	0.218
	N2	2	0.2
Total		8	1.3
$BaTiN_2$	Ba	2	0.2
	Ti	2	0.1
	N1	2	0.204
	N2	2	0.202
Total		8	1.4

5 G. J. Snyder and E. S. Toberer, *Nat Mater*, 2008, **7**, 105–114.

6 J. Sootsman, D. Chung and M. Kanatzidis, *Ang. Chem. Inter. Ed.*, 2009, **48**, 8616–8639.

7 N. A. Mecholsky, L. Resca, I. L. Pegg and M. Fornari, *Phys. Rev. B*, 2014, **89**, 155131.

8 T. M. Tritt and M. A. Subramanian, *MRS bulletin*, 2006, **31**, 199.

9 G. D. Mahan and J. O. Sofo, *Proceedings of the National Academy of Sciences*, 1996, **93**, 7436–7439.

10 D. J. Singh, in *Chapter 5 Theoretical and computational approaches for identifying and optimizing novel thermoelectric materials*, ed. T. M. Tritt, Elsevier, 2001, vol. 70, pp. 125 – 177.

11 D. Singh, *Phys. Rev. B: Condens. Matter Mater. Phys.*, 2010, **81**, 195217.

12 S. Hui, M. D. Nielsen, M. R. Homer, D. L. Medlin, J. Tobola, J. R. Salvador, J. P. Heremans, K. P. Pipe and C. Uher, *J. Appl. Phys.*, 2014, **115**, 103704.

13 T. M. Tritt, *Thermal Conductivity : Theory, Properties, and Applications*, Springer Series in Physics of Solids and Liquids, 2004.

14 G. S. Nolas, D. T. Morelli and T. M. Tritt, *Ann. Rev. Mater. Sci.*, 1999, **29**, 89–116.

15 B. C. Sales, D. Mandrus and R. K. Williams, *Science*, 1996, **272**, 1325–1328.

16 D. Wee, B. Kozinsky, N. Marzari and M. Fornari, *Phys. Rev. B: Condens. Matter Mater. Phys.*, 2010, **81**, 045204.

17 T. Zhou, B. Lenoir, M. Colin, A. Dauscher, R. A. R. Al Orabi, P. Gougeon, M. Potel and E. Guilmeau, *Appl. Phys. Lett.*, 2011, **98**, 162106.

18 P. Gougeon, P. Gall, R. Al Rahal Al Orabi, B. Fontaine, R. Gautier, M. Potel, T. Zhou, B. Lenoir, M. Colin, C. Candolfi and A. Dauscher, *Chem. Mater.*, 2012, **24**, 2899–2908.

19 G. S. Nolas, J. L. Cohn, G. A. Slack and S. B. Schujman, *Appl. Phys. Lett.*, 1998, **73**, 178–180.

20 E. S. Toberer, M. Christensen, B. B. Iversen and G. J. Snyder, *Phys. Rev. B: Condens. Matter Mater. Phys.*, 2008, **77**, 075203.

21 D. Singh and I. Mazin, *Phys. Rev. B: Condens. Matter Mater. Phys.*, 1997, **56**, R1650–R1653.

22 R. Al Rahal Al Orabi, P. Gougeon, P. Gall, B. Fontaine, R. Gautier, M. Colin, C. Candolfi, A. Dauscher, J. Hejtmanek, B. Malaman and B. Lenoir, *Inor. Chem.*, 2014, **53**, 11699–11709.

23 D. Morelli, J. Heremans and G. Slack, *Phys. Rev. B: Condens. Matter Mater. Phys.*, 2002, **66**, 195304.

24 Y. Ma, Q. Hao, B. Poudel, Y. Lan, B. Yu, D. Wang, G. Chen and Z. Ren, *Nano Lett.*, 2008, **8**, 2580–2584.

25 A. J. Minnich, M. S. Dresselhaus, Z. F. Ren and G. Chen, *Energy Environ. Sci.*, 2009, **2**, 466–479.

26 L. W. A. Datta, A. Popescu and G. Nolas, *The bottom-up approach to bulk thermoelectric materials with nano-scale domains’, in CRC Handbook on Thermoelectrics and Its Energy Harvesting on Materials, Preparation and Characterization*, 2012.

27 M. G. Kanatzidis, *Chem. Mater.*, 2010, **22**, 648–659.

28 K. F. Hsu, S. Loo, F. Guo, W. Chen, J. S. Dyck, C. Uher, T. Hogan, E. K. Polychroniadis and M. G. Kanatzidis, *Science*, 2004, **303**, 818–821.

29 B. Poudel, Q. Hao, Y. Ma, Y. Lan, A. Minnich, B. Yu, X. Yan, D. Wang, A. Muto, D. Vashaee, X. Chen, J. Liu, M. S. Dresselhaus, G. Chen and Z. Ren, *Science*, 2008, **320**, 634–638.

30 J. He, I. D. Blum, H.-Q. Wang, S. N. Girard, J. Doak, L.-D. Zhao, J.-C. Zheng, G. Casillas, C. Wolverton, M. Jose-Yacaman, D. N. Seidman, M. G. Kanatzidis and V. P. Dravid, *Nano Lett.*, 2012, **12**, 5979–5984.

31 M. Lee, L. Viciu, L. Li, Y. Wang, M. L. Foo, S. Watauchi, R. A. Pascal Jr, R. J. Cava and N. P. Ong, *Nat Mater*, 2006, **5**, 537–540.

32 I. Terasaki, Y. Sasago and K. Uchinokura, *Phys. Rev. B: Condens. Matter Mater. Phys.*, 1997, **56**, R12685–R12687.

33 K. Koumoto, R. Funahashi, E. Guilmeau, Y. Miyazaki, A. Weidenkaff, Y. Wang and C. Wan, *J. Am. Ceram. Soc.*, 2013, **96**, 1–23.

34 Y.-L. Pei, H. Wu, D. Wu, F. Zheng and J. He, *J. Amer. Chem. Soc.*, 2014, **136**, 13902–13908.

35 L.-D. Zhao, J. He, D. Berardan, Y. Lin, J.-F. Li, C.-W. Nan and N. Dragoe, *Energy Environ. Sci.*, 2014, **7**, 2900–2924.

36 G. Wilson-Short, D. Singh, M. Fornari and M. Suewattana, *Phys. Rev. B: Condens. Matter Mater. Phys.*, 2007, **75**, 035121.

37 P. Vaqueiro, S. D. N. Luu, G. Guelou, A. V. Powell, R. I. Smith, R. Al Rahal Al Orabi, J.-P. Song, D. Wee and M. Fornari, *in preparation*.

38 S. Yamanaka, K.-i. Hotehama and H. Kawaji, *Nature*, 1998, **392**, 580–582.

39 A. Fuertes, M. Vlassov, D. Beltrn-Porter, P. Alemany, E. Canadell, N. Casa-Pastor and M. R. Palacn, *Chem. Mater.*, 1999, **11**, 203–206.

40 A. Zerr, G. Miehe, G. Serghiou, M. Schwarz, E. Kroke, R. Riedel, H. Fuesz, P. Kroll and R. Boehler, *Nature*, 1999, **400**, 340–342.

41 N. Scotti, W. Kockelmann, J. Senker, S. Trael and H. Jacobs, *Z. Ano. All. Chem.*, 1999, **625**, 1435–1439.

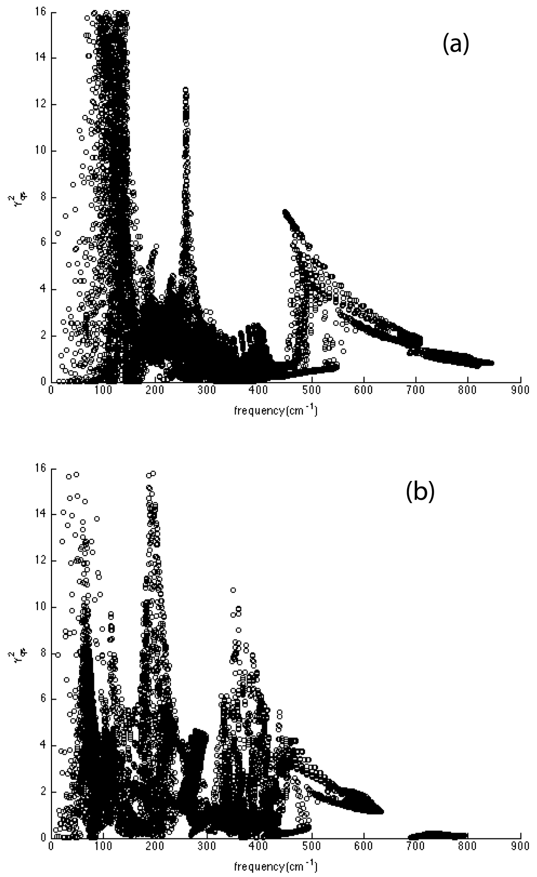

Fig. 11 Mode-resolved Grüneisen parameters versus mode frequency for $CaTiN_2$ (a) and $BaTiN_2$ (b).

42 D. H. Gregory, M. G. Barker, P. P. Edwards and D. J. Siddons, *Inorg. Chem.*, 1998, **37**, 3775–3778.

43 M. Y. Chern and F. Disalvo, *J. Solid State Chem.*, 1990, **88**, 459 – 464.

44 D. Gregory, M. Barker, P. Edwards, M. Slaski and D. Siddons, *J.Solid State Chem.*, 1998, **137**, 62 – 70.

45 G. Farault, R. Gautier, C. F. Baker, A. Bowman and D. H. Gregory, *Chem. Mater.*, 2003, **15**, 3922–3929.

46 I. Ohkubo and T. Mori, *Chem. Mater.*, 2014, **26**, 2532.

47 P. Blaha, K. Schwarz, G. K. H. Madsen, D. Kvasnicka and J. Luitz, *WIEN2K, An Augmented Plane Wave + Local Orbitals Program for Calculating Crystal Properties*, Karlheinz Schwarz, Techn. Universität Wien, Austria, 2001.

48 J. P. Perdew, K. Burke and M. Ernzerhof, *Phys. Rev. Lett.*, 1997, **78**, 1396–1396.

49 F. Tran and P. Blaha, *Phys. Rev. Lett.*, 2009, **102**, 226401.

50 F. Birch, *Phys. Rev.*, 1947, **71**, 809–824.

51 F. D. Murnaghan, *Proc. Nat. Acad. Sci.*, 1944, **30**, 244–247.

52 T. J. Scheidemantel, C. Ambrosch-Draxl, T. Thonhauser, J. V. Badding and J. O. Sofo, *Phys. Rev. B: Condens. Matter Mater. Phys.*, 2003, **68**, 125210.

53 G. K. H. Madsen, *J. Am. Chem. Soc.*, 2006, **128**, 12140–12146.

54 G. K. Madsen and D. J. Singh, *Comp. Phys. Commun.*, 2006, **175**, 67 – 71.

55 S. Baroni, S. de Gironcoli, A. Dal Corso and P. Giannozzi, *Rev. Mod. Phys.*, 2001, **73**, 515–562.

56 P. Giannozzi and et al, *J. Phys. : Condens. Matter*, 2009, **21**, 395502.

57 D. Vanderbilt, *Phys. Rev. B: Condens. Matter Mater. Phys.*, 1990, **41**, 7892–7895.

58 K. F. Garrity, J. W. Bennett, K. M. Rabe and D. Vanderbilt, *Comp. Mater. Sci.*, 2014, **81**, 446 – 452.

59 J. P. Perdew, A. Ruzsinszky, G. I. Csonka, O. A. Vydrov, G. E. Scuseria, L. A. Constantin, X. Zhou and K. Burke, *Phys. Rev. Lett.*, 2008, **100**, 136406.

60 O. Seeger, M. Hofmann, J. Strhle, J. P. Laval and B. Frit, *Anorg. All. Chem.*, 1994, **620**, 2008–2013.

61 A. Kaur, E. Ylvisaker, Y. Li, G. Galli and W. Pickett, *Phys. Rev. B: Condens. Matter Mater. Phys.*, 2010, **82**, 155125.

62 A. Filippetti, P. Delugas, M. Verstraete, I. Pallecchi, A. Gadaleta, D. Marré, D. Li, S. Gariglio and V. Fiorentini, *Phys. Rev. B: Condens. Matter Mater. Phys.*, 2012, **86**, 195301.

63 N. A. Mecholsky, B. Hamad, L. Resca, I. L. Pegg and M. Fornari, *Energy Harvesting and Systems*, 2014, **in press**,.

64 S. Ganesan, *Philos. Mag.*, 1962, **7**, 197–205.

65 D. T. Morelli, V. Jovovic and J. P. Heremans, *Phys. Rev. Lett.*, 2008, **101**, 035901.

66 J. Y. Cho, X. Shi, J. R. Salvador, G. P. Meisner, J. Yang, H. Wang, A. A. Wereszczak, X. Zhou and C. Uher, *Phys. Rev. B: Condens. Matter Mater. Phys.*, 2011, **84**, 085207.

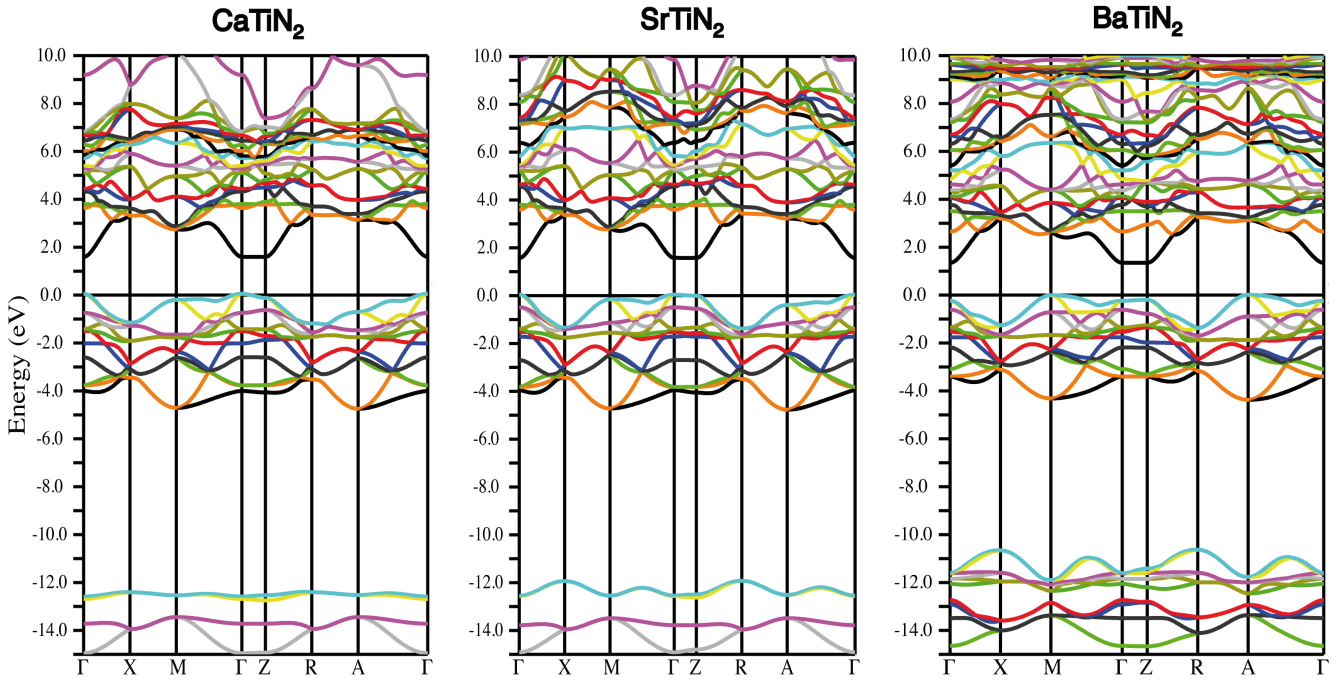

Fig. 2 Band structure for CaTiN$_2$, SrTiN$_2$ and BaTiN$_2$. Energies are refereed to the top of the valence band (black solid lines at 0 eV).

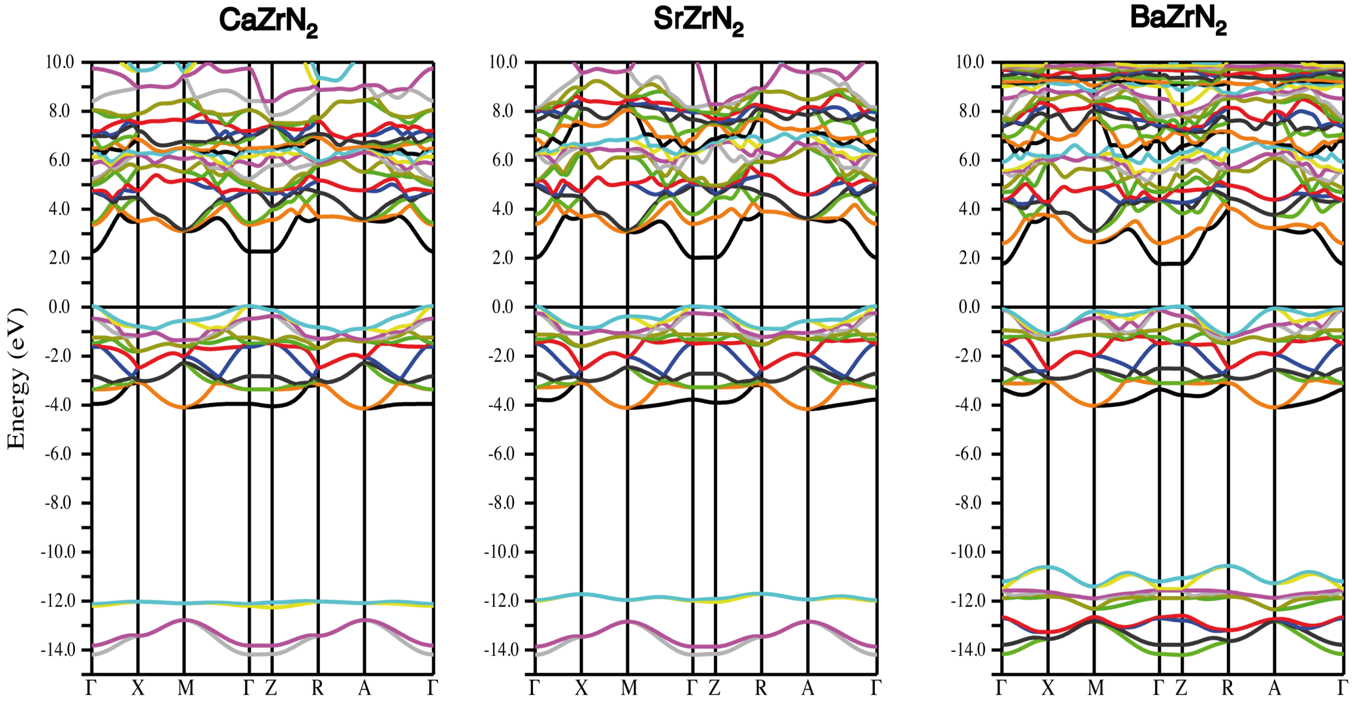

Fig. 3 Band structure for CaZrN$_2$, SrZrN$_2$ and BaZrN$_2$. Energies are refereed to the top of the valence band (black solid lines at 0 eV).

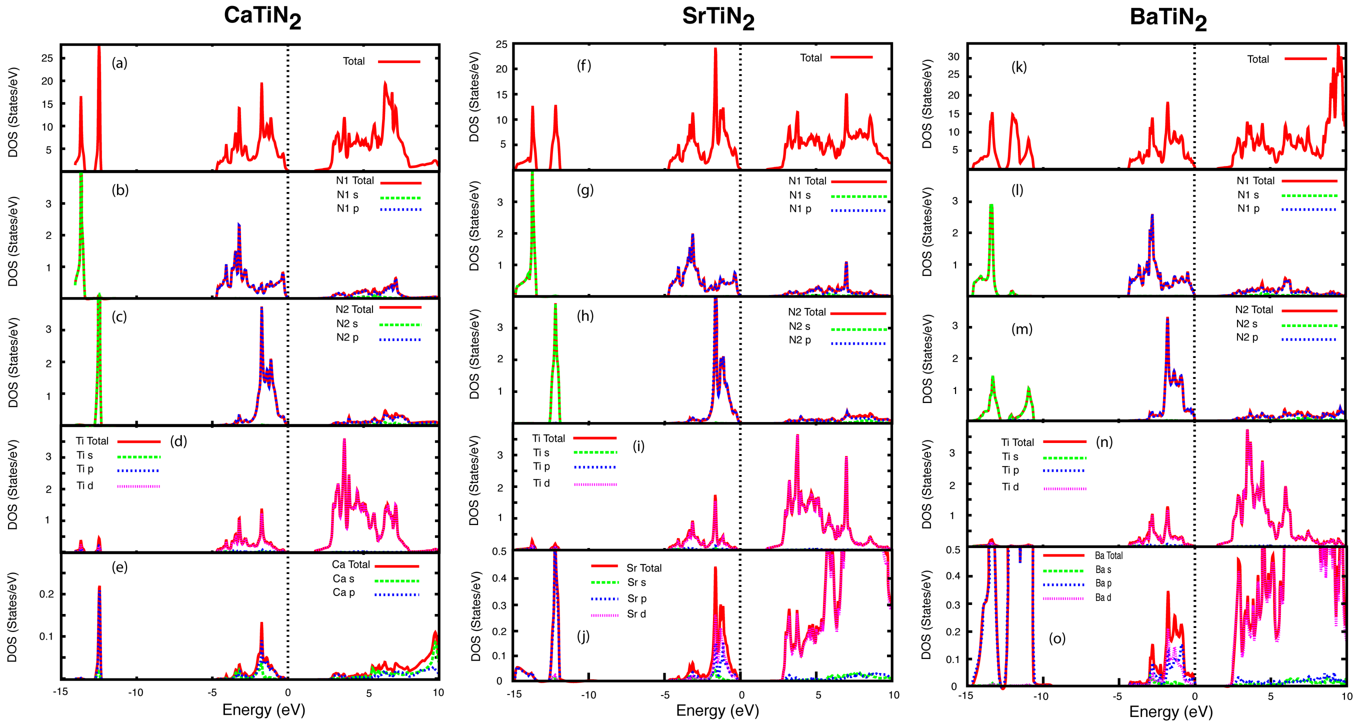

Fig. 4 Density of states projected on the atomic spheres for $CaTiN_2$, $SrTiN_2$ and $BaTiN_2$. Energies are refereed to the top of the valence band.

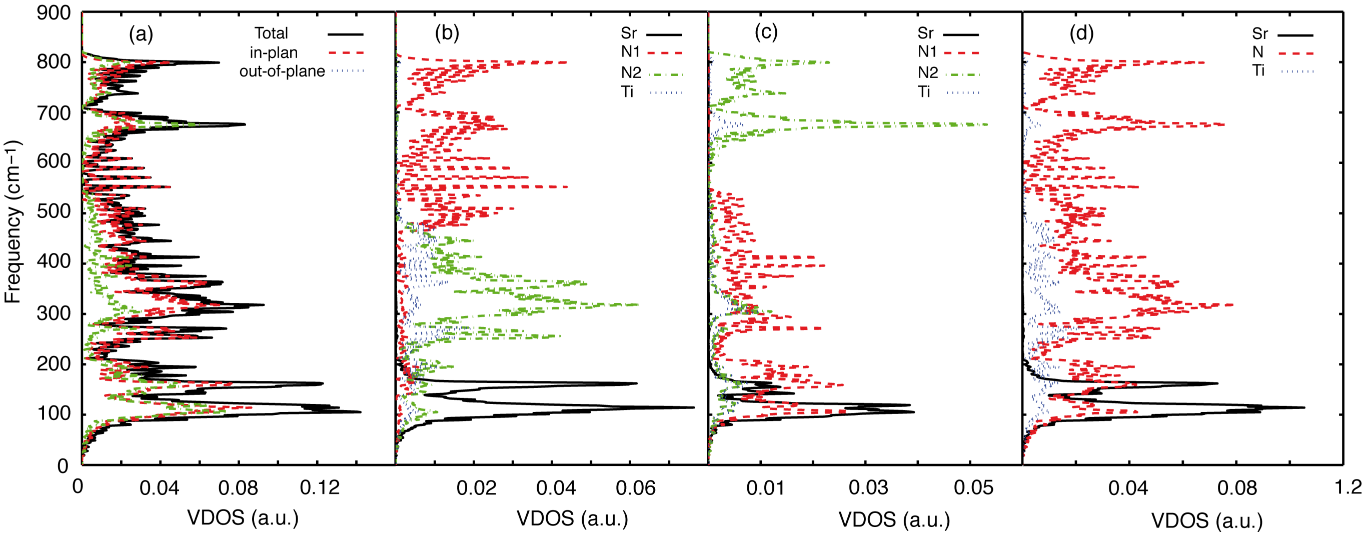

Fig. 9 Vibration density of states of $SrTiN_2$. (a) Total, in-plane, and out-of-plane VDOSs; (b) in-plane VDOS projected on each element; (c) out-of-plane VDOS projected on each element; (d) total VDOS projected on each element.

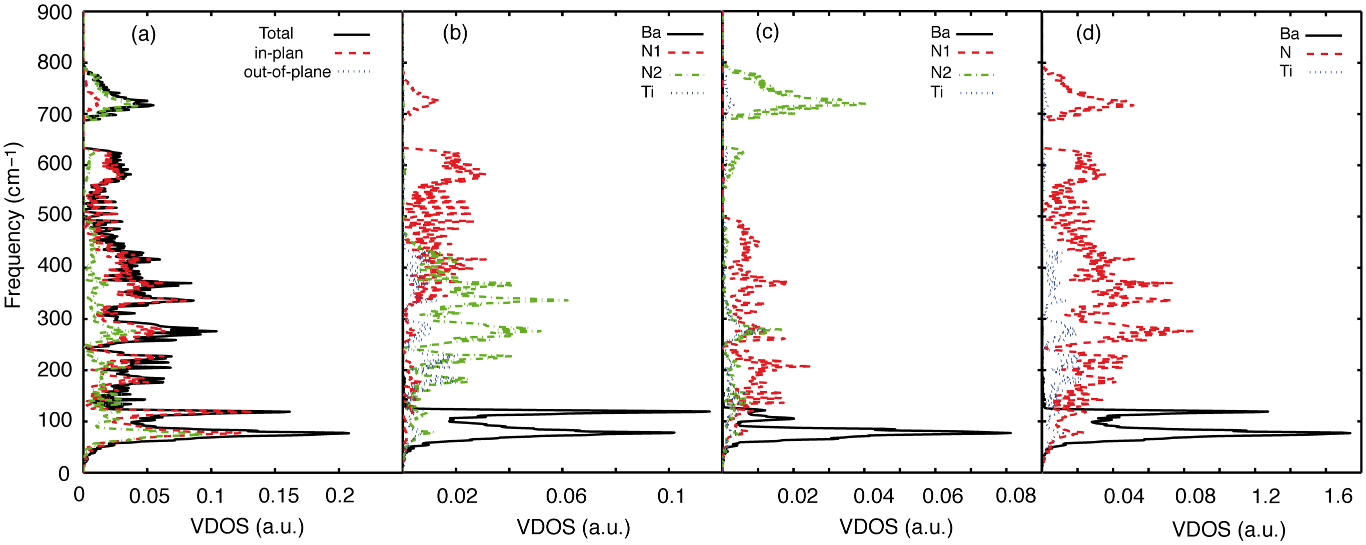

Fig. 10 Vibration density of states of $BaTiN_2$. (a) Total, in-plane, and out-of-plane VDOSs; (b) in-plane VDOS projected on each element; (c) out-of-plane VDOS projected on each element; (d) total VDOS projected on each element.

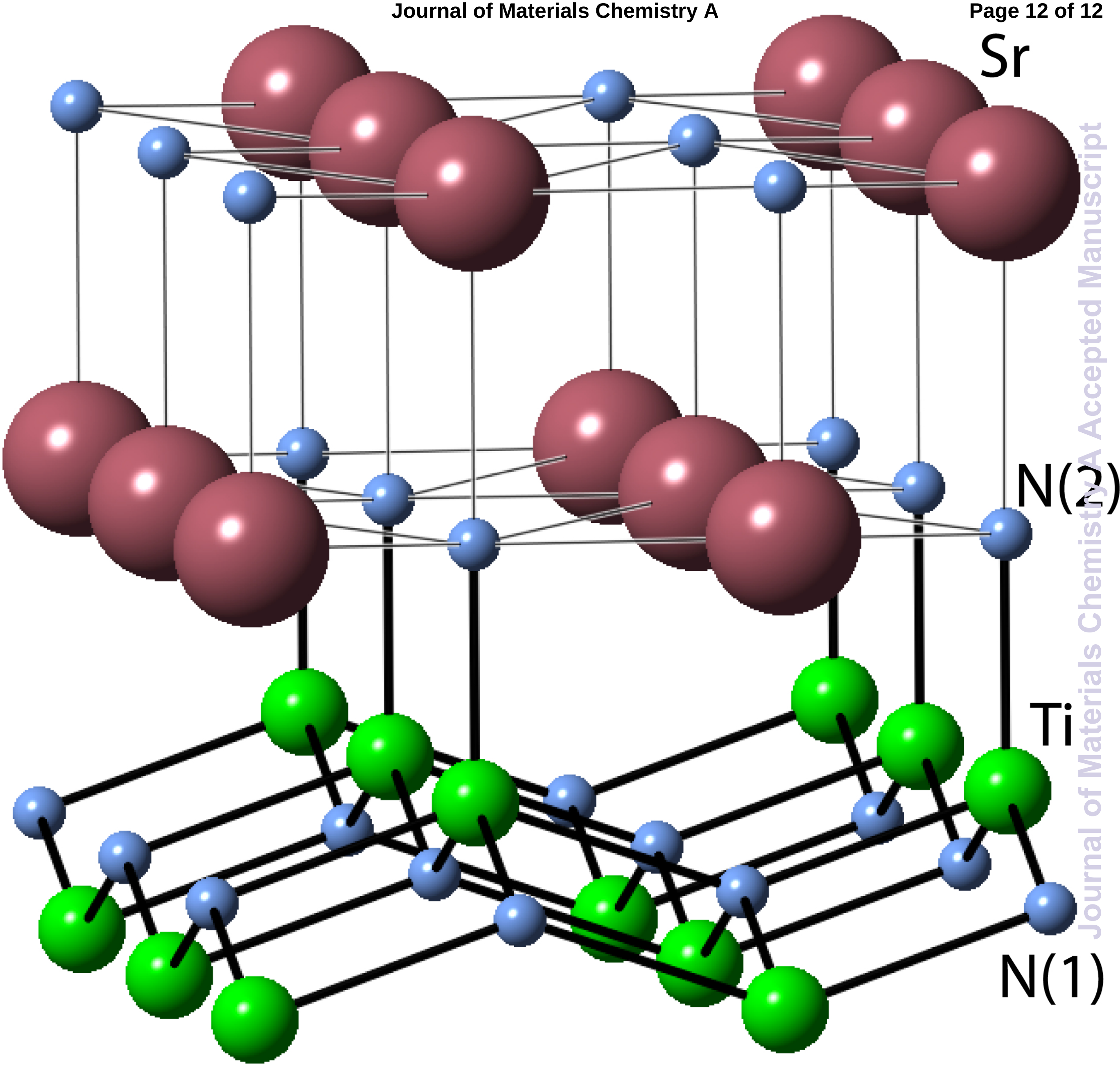
Sr
N(2)
Ti
N(1)